RSC Advances

PAPER

View Article Online
View Journal | View Issue

Cite this: RSC Adv., 2023, 13, 26213

Retama monosperma chemical profile, green synthesis of silver nanoparticles, and antimicrobial potential: a study supported by network pharmacology and molecular docking

Mohammad H. Alyami,[a] Amal M. Fakhry,[b] Nancy M. El Halfawy,[b] Soliman M. Toto,[b] Nada K. Sedky,[c] Heba A. Yassin,[d] Sherif Ashraf Fahmy*[e] and Fatma A. Mokhtar[f]

Received 28th July 2023
Accepted 22nd August 2023

DOI: 10.1039/d3ra05116a

rsc.li/rsc-advances

In this study, *Retama monosperma* extract (RME) was used for the green synthesis of silver nanoparticles (RME-AgNPs). RME's phenolic profile was identified by liquid chromatography coupled to mass spectroscopy (LC-ESI/MS/MS) technique. A tentative identification of 21 phenolic metabolites from the extract was performed. The produced RME-AgNPs showed UV absorbance at 443 nm. FTIR spectroscopy confirmed the presence of RME functional groups. In addition, XRD analysis confirmed the crystallography of RME-AgNPs *via* exhibiting peaks with 2θ values at 38.34°, 44.29°, and 64.65°. RME-AgNPs were spherical with particle sizes ranging from 9.87 to 21.16 nm, as determined by SEM and HR-TEM techniques. The zeta potential determined the particle's charge value as −15.25 mv. RME-AgNPs exhibited significantly higher antibacterial activity against Gram-negative (*Escherichia coli*, *Pseudomonas aeruginosa*, Serratia *marcescens*, and *Klebsiella pneumoniae*) and Gram-positive bacteria (*Bacillus subtilis* and *Staphylococcus aureus*) compared to RME. Moreover, the SEM images of green-synthesized nanoparticles revealed severe damage and deformation in the bacterial cell wall of the different strains subjected to the current investigation. The bioinformatics study identified 266 targets, among which only 41 targets were associated with bacterial infections. The PI3K-Akt and Relaxin signaling pathways were the top KEGG signaling pathways. Molecular docking was also performed for the 21 identified compounds at the TNF-α active site; kaempferol-3-*O*-robinoside-7-*O*-rhamnoside had a higher binding energy (−6.8084). The findings of this study warrant the use of green-synthesized AgNPs from *Retama monosperma* as potential antibacterial agents.

1. Introduction

The emergence of antimicrobial resistance (AMR) is a severe worldwide problem that has led to deterioration in human health and economic development. Poverty, poor sanitation, antibiotic administration abuse, and disregarding clinical practice protocols are among several factors that aid in spreading multidrug-resistant (MDR) microbial strains.[1] Thus, a global demand exists to innovate alternative therapies to traditional antibiotics that could tackle the MDR issue.[2]

Chemically synthesized metallic nanoparticles (MNPs), including silver nanoparticles (Ag NPs), have attracted attention as promising therapeutic candidates in various biomedical applications However, their biomedical applications are hindered by their toxicity and highly persistent nature in the environment. Accordingly, medicinal plants are exploited for the green synthesis of MNPs, becoming an eco-friendly and benign source of therapeutic MNPs.[3] Medicinal plants contain various phytochemicals such as polyphenols, flavonoids, alkaloids, coumarins, and terpenoids that serve as natural reductants and capping agents, facilitating the nano-sizing of NPs, diminishing their high surface energy and inhibiting their aggregation.[4,5] In addition, many of these phytochemicals are biologically active compounds that possess bactericidal activities against MDR pathogenic bacteria.[6,7]

Retama monosperma (L.) Boiss. is a branched shrub that grows in the Mediterranean regions (belongs to the *Fabaceae*

---

[a] Department of Pharmaceutics, College of Pharmacy, Najran University, Najran 66462, Saudi Arabia

[b] Department of Botany & Microbiology, Faculty of Science, Alexandria University, Alexandria 21511, Egypt

[c] Department of Biochemistry, School of Life and Medical Sciences, University of Hertfordshire Hosted By Global Academic Foundation, R5 New Garden City, New Capital, Cairo 11835, Egypt

[d] School of Pharmacy, Pharmaceutics Department, Badr University in Cairo (BUC), Egypt

[e] Department of Chemistry, School of Life and Medical Sciences, University of Hertfordshire Hosted By Global Academic Foundation, R5 New Garden City, New Capital, Cairo 11835, Egypt. E-mail: sheriffahmy@aucegypt.edu

[f] Department of Pharmacognosy, Faculty of Pharmacy, El Saleheya El Gadida University, El Saleheya El Gadida, Sharkia, 44813, Egypt

family), which has been used in traditional medicine to treat various diseases, including diabetes, abortion, rheumatism, and hypertension.[8,9] In addition, several studies reported the biological activities of *R. monosperma*, including antibacterial, anti-inflammatory, antioxidant, anti-proliferative, antiulcer, antiviral, and hepatoprotective activities.[10,11] Moreover, the roots of *R. monosperma* are reported to contain natural antioxidants, including flavonoids and phenolic compounds, making them promising candidates for the green synthesis of MNPs, including AgNPs.[10]

Silver nanoparticles (AgNPs) are attracting attention as potential antibacterial agents due to their intriguing physicochemical features and innate ability to penetrate bacterial cell walls, altering the construction of cell membranes and even leading to cell death. In addition, their nanoscale sizes and large surface area-to-volume ratio improve their capability to cross cell membranes, releasing silver ions intracellularly, leading to the generation of reactive oxygen species and interfering with deoxyribonucleic acid replication.[12–14]

In this study, a facile and environment-friendly method was utilized to synthesize AGNPs using the root extract of *R. monosperma*. The green-synthesized nanoparticles were investigated for antibacterial activities against different human pathogens. In addition, network pharmacology and *in silico* molecular docking studies were conducted to explore the possible genes responsible for the antimicrobial activity and the signaling pathways in a computational bioinformatics manner.

2. Materials and methods

2.1. Chemicals

$AgNO_3$, chemicals, and solvents were purchased from Sigma-Aldrich (St. Louis, MO).

2.2. Plant material

The roots of *R. monosperma* were collected from the northern coast of Egypt in January 2022. The plant was identified by Selim Z. Heneidy, professor of Flora and Ecology, Department of Botany and Microbiology, Faculty of Science, Alexandria University. A voucher specimen was deposited at the Herbarium of the Botanic Garden (Heneidy *et al.* Collection, serial no. 6505).

2.3. Plant extraction

The roots of *Retama monosperma* were thoroughly washed several times with distilled water, sliced, shade-dried, and grounded to a fine powder. Then, 100 g powder was extracted in 80% ethanol/H_2O (1 L) in triplicate, each time for two days, the extracted solution was evaporated under vacuum at 45 °C to yield 13.2 g dry weight extract.

2.4. LC-ESI-MS/MS

Liquid chromatography-electrospray ionization-tandem mass spectrometry (LC-ESI-MS/MS) analysis was performed in the Proteomics and Metabolomics Research Program CCHE 57357. The sample was prepared in a reconstitution solvent composed of water : methanol : acetonitrile in a ratio of 50 : 25 : 25, V/V, 50 mg of the sample was dissolved in 1 mL of the reconstitution solvent, vortexed for 2 min, ultrasonicated for 10 min, and then centrifuged at 10 000 rpm for 10 min. The injected concentration was 2.5 $\mu g\ \mu L^{-1}$, and the sample was injected in negative mode and again injected in positive mode. Data were processed using MS-DIAL 4.8, and the used reference databases were: ReSpect negative and ReSpect positive. The MasterView software was used for feature (peaks) extraction from total ion chromatogram (TIC).

2.5. Green synthesis of AgNPs

A solution of 0.1 M $AgNO_3$ was freshly prepared and preserved in an ambient closed glass container, then, 100 mL of aqueous solution of the *R. monosperma* extract (RME, 10 g L^{-1}) was added to a freshly prepared $AgNO_3$ solution (0.1 M), mixed well, and kept in a dark place. The mixed solution was observed for physical appearance changes every 15 minutes to check the end of the reaction. After the reaction was complete, the resulting mixture was centrifuged at 3000 rpm for 30 min and then washed 3 times with deionized water, followed by washing with absolute ethanol for three times. The formed nanoparticles were immediately dried at room temperature.

2.6. Characterization of the formed nanoparticles

2.6.1. Physical observation. The formation of silver nanoparticles was indicated by the change in turbidity, fluorescence, precipitate formation or color of the mixture solution.

2.6.2. UV-vis spectrophotometry. A UV-spectrophotometer (Shimadzu, Kyoto, Japan) was used to confirm the formation of AgNPs.

2.6.3. FTIR spectroscopy. The different functional groups of biogenic AgNPs and plant extract were measured using a PerkinElmer system 2000 instrument. The spectra for each sample were scanned three times, and the average values of percent transmittance were plotted against wavelength (4000–400 cm^{-1}).[15]

2.6.4. XRD. XRD analysis was performed using a surface chemical analysis tool to characterize metal nanoparticles. This analysis was performed using an XRD-6000 detector from Shimadzu, Japan, utilizing a monochromatic Cu-Kα radiation source ($\theta = 1.5406$ Å) at 45 kV and 30 mA at ambient temperature. The silver nano-powder intensity data were gathered over a 2θ range of 4.01°–79.99°.

2.6.5. Zeta potential. The particle stability and homogeneity of distribution, and zeta potentials of biogenic AgNPs were examined using a zeta sizer analyzer manufactured by Malvern Panalytical Ltd Model of NanoSight NS500 (**https://www.malvernpanalytical.com/en/support/product-support/nanosight-range/nanosight-ns500**).[16]

2.7. Microbiological study

2.7.1. Disk diffusion assay. The antibacterial activity of RME and RME-AgNPs was studied by Kirby-Bauer Disk Diffusion Susceptibility Test[17] against Gram-negative bacteria *Escherichia coli* (ATCC 8739), *Pseudomonas aeruginosa* (ATCC

27853), Serratia *marcescens* (ATCC 14756), and *Klebsiella pneumoniae* (ATCC 13883) and Gram-positive bacteria *Staphylococcus aureus* (ATCC 25923) and *Bacillus subtilis* (ATCC 6633). The bacterial strains were grown on a Mueller–Hinton agar (MHA; HiMedia, India) medium at 37 °C for 18 h. MHA plates were prepared by inoculating bacterial strains with a final inoculum size of $\sim 10^6$ CFU mL^{-1}. Sterile blank antimicrobial susceptibility disks were placed on agar plates, loaded with 50 μL of sterile suspension solution with a final concentration of 500 μg mL^{-1} and incubated at 37 °C for 24 h. The activity was determined by measuring the diameter of the inhibition zone in millimetres (mm). Antibiotic ampicillin (10 mg mL^{-1}) was used as a positive control, while sterile deionized water was used as a negative control. This assay was performed in replica for each bacterial strain, and the data are expressed as mean ± standard deviation (SD).

2.7.2. Minimum inhibitory concentration (MIC) and minimum bactericidal concentration (MBC) assays. Minimum inhibitory concentration (MIC) and minimum bactericidal concentration (MBC) were determined by a broth microdilution method according to the Clinical and Laboratory Standards Institute.[18] Stock solutions of RME extract were prepared in deionized water and sterilized using a 0.22 μm filter. Sequential 2-fold serial dilutions were prepared in 96-well polystyrene microtiter plates ranging from 2048 to 1 μg mL^{-1} using Mueller–Hintor broth (MHB) and inoculated with 50 μL bacterial inoculum adjusted to a concentration of 10^6 CFU mL^{-1}. Plates were incubated aerobically at 37 °C for 24 h. The MIC value is defined as the concentration of the complex at which bacteria reveal no observable growth, while MBC is the complex concentration that prevented the growth of any bacteria after plating 50 μL from the wells onto MHA plates. The reported MIC and MBC data resulted from three independent assays.

2.7.3. Time-killing assay of RME-AgNPs. Bacterial growth kinetics was measured spectrophotometrically at OD_{600} using a cell density meter (Fisherbrand™) in the presence of different concentrations of green-synthesized RME-AgNPs. The experiment was conducted by inoculating 50 mL MHB flasks with 1% (v/v) diluted bacterial cultures ($\sim 10^8$ CFU mL^{-1}) supplemented with RME-AgNPs. Flasks containing cultures were incubated aerobically using a shaker incubator at 37 °C and 150 rpm. Bacterial growth was measured at different time intervals (up to 24 h), and flasks without RME-AgNPs were used as the control. For all the growth curve measurements, two replicates were carried out.

2.7.4. Scanning electron microscopy (SEM) of bacteria. To study the morphological changes of targeted bacterial cells (*B. subtilis*, *S. aureus*, *E. coli*, *P. aeruginosa*) after treatment with RME-AgNPs, they were cultivated in LB broth until OD_{600} of 0.2 at 37 °C and 150 rpm. Bacterial cells were collected by centrifugation at 4000 rpm for 10 min and washed twice with sterile deionized water. Bacterial pellets were treated with a RME-AgNP solution for 12 h. Samples were fixed with a 5% glutaraldehyde solution and then coated with gold (15 A) for 2 min by physical vapor deposition before visualization at an accelerating voltage of 20.0 kV. The samples were visualized by scanning electron microscopy (SEM; JSM-IT 200, JEOL, Japan), EM Unit, Alexandria University, Egypt.

2.8. Bioinformatics study

2.8.1. Plant-compound networks. Metabolic profiling was identified based on the chemical analysis of Retama monosperma using LC/MS/MS, and the identified compounds were connected to the *Retama monosperma* extract in a simple network.

2.8.2. Compound-target networks. A network was constructed between the identified compounds from RME and annotated targets. The target genes annotated by the identified compounds were predicted using the PubChem database (**https://pubchem.ncbi.nlm.nih.gov/**)[19] (last accessed on 1-03-2023), UniProtKB/Swiss-Prot database (**https://www.uniprot.org/help/uniprotkb**)[20] last accessed on (12-03-2023) and SwissTargetPrediction database (**https://www.swisstargetprediction.ch/**)[21] (last accessed on 7-04-2023), the top target genes were selected based on similarity index of more than 0.7 in BindingDB and the top targets were chosen in the SwissTargetPrediction database using canonical smiles for each structure as the input data method; the human species (*Homo sapien*) was selected.

2.8.3. Complete network pharmacology (plant-compound-target). A complete network pharmacology was obtained by merging the two networks (plant-compounds) and (compound-targets).

2.8.4. Target-bacterial infection networks. A network of all the identified targets was formed, and the common bacterial infections were identified using the DisGeNET database (**https://www.disgenet.org/**)[22] (Last accessed on 10-04-2023). DisGeNET results were filtered using the words "infection", and "bacteria" to focus on common bacterial infections.

2.8.5. Infection target-compound networks. The targets related to bacterial infections were used to construct a network in a backward way. A network was constructed to connect bacterial infections to the compounds identified from the *Retama monosperma* plant.

2.8.6. (Infection–infection target-compound) networks. A network was formed by merging the target-bacterial infection and (infection target-compound networks. The formed network was called the infection–infection target compound) network. This network was constructed to identify the top compounds with antimicrobial activities.

2.8.7. Network construction. Network construction, visual types of bacterial infections, and analysis were performed using Cytoscape software 3.9.0. Nodes represent plant names (*Retama monosperma*), targets, and compounds in the graphical network. The edges represent corresponding interactions.

2.8.8. Gene enrichment analysis. The represented pathways of the targets of *Retama monosperma* related to bacterial infections were retrieved using the ShinyGO database **https://bioinformatics.sdstate.edu/go76/** (ref. 23) (last accessed on 14-04-2023). ShinyGO database allowed the identification of KEGG biological pathways, gene ontology analysis in terms of biological process, cellular components, and molecular function.

2.9. Molecular docking study

2.9.1. Protein and test set preparation for docking. As TNF gene was the top reported gene against Gram-positive and

Gram-negative bacterial infections, *Retama monosperma* extract 21 compounds were evaluated *in silico* against the TNF-α receptor to determine the main components responsible for the reported antimicrobial activity. The TNF-α crystal structure (PDB ID: 2AZ5) (**https://www.rcsb.org/structure/2az5**) in complex with a small-molecule inhibitor was downloaded from the Protein Data Bank. The employed preparation protocol is similar to previous recent studies conducted on the same PDB ID. AutoDock was used to prepare protein structures using prepare_receptor4.py command of the ADT to remove water molecules, add polar hydrogens, and minimize the structure energy and then saved in the PDBQT format.

For ligands, the chemical structures of *Retama monosperma* extract were extracted from the PubChem database in the SDF format and then converted into the PDBQT format using the Open Babel software[24] while being prepared using prepare_ligand4.py command in AutoDockTools (ADT, v1.5.6).[25]

2.9.2. Redocking of the co-crystallized ligands and virtual screening of test sets. Docking was carried out in the same co-crystallized ligand docking site, where the grid box was set to 66 in *x*, *y* and *z* directions. To validate the docking performance, root mean square deviation (RMSD) values between the docked conformation and the reference conformation of co-crystallized ligand expresses in Å were utilized.[26] The Lamarckian genetic algorithm was used for setting docking parameters, where ten binding poses are retrieved for each ligand.[27] Two-dimensional interaction figures of best scored ligands were generated using BIOVA Discovery Studio visualizer 2021.

3. Results and discussion

3.1. LC-ESI/MS/MS analysis

Phenolic profiling of RME was investigated tentatively by LC-ESI/MS/MS analysis in the negative ion mode, based on [M–H] of the compounds and fragmentation pattern of each compound. The LC-ESI-MS/MS analysis tentatively identified 21 phenolic compounds; 17 flavonoids, 2 phenolic acids, 1 anthraquinone and 1 aldehyde. Caffeic acid and *p*-hydroxybenzoic acid were identified at *m*/*z* $[M-H]^-$ 179.05 and 137.02, respectively. Syringaldehyde was identified at $[M-H]^-$ 181.05, and the identified anthraquinone was cyanidin-3,5-di-*O*-glucoside at *m*/*z* $[M-H]^-$ 609.15. The identified flavonoids are 5 aglycones and 12 flavonoid glycosides. The flavonoid glycosides are mainly kaempferol derivatives and quercetin derivatives, luteolin-6-*C*-glucoside and daidzein-8-*C*-glucoside, myricitrin, and acacetin-7-*O*-rutinoside. The identified kaempferol derivatives at *m*/*z* $[M-H]^-$ 577.16, 593.15, 739.21, 477.09, 593.05, and 431.10 corresponding to kaempferol-3,7-*O*-bis-alpha-L-rhamnoside, kaempferol-3-*O*-(6''''-*p*-coumaroyl)-glucoside, kaempferol-3-*O*-robinoside-7-*O*-rhamnoside, kaempferol-3-*O*-glucoside, kaempferol-7-neohesperidoside, and kaempferol-3-*O*-alpha-L-rhamnoside in the same order. Quercetin derivatives were quercetin-3-*O*-arabinoglucoside and quercetin-4′-glucoside at *m*/*z* $[M-H]^-$ 595.02 and 463.12, respectively. The identified aglycones are quercetin at *m*/*z* $[M-H]^-$ 301.01, luteolin at *m*/*z* $[M-H]^-$ 285.04, apigenin at *m*/*z* $[M-H]^-$ 269.04, acacetin at *m*/*z* $[M-H]^-$ 283.02, and naringenin at *m*/*z* $[M-H]^-$ 271.06 (Fig. 1, 2 and Table 1).

3.2. Characterization of silver nanoparticles synthesized by RME (RME-AgNPs)

3.2.1. UV-Vis spectrophotometry. The biosynthesis of AgNPs mediated by RME was tracked visually and by UV-Vis spectrophotometry. Primarily, the creation of the RME-AgNPs was confirmed qualitatively by the gradual color change from green to a brownish turbid solution. Then, the generation of green-synthesized AgNPs was further confirmed by UV-Vis spectrophotometry (Fig. 3). A significant surface plasmon resonance peak was remarked at 443 nm for AGNPs. These findings indicated the bioreduction of the silver nitrate solution into AgNPs.

3.2.2. Fourier-transform infrared (FTIR) spectroscopy. FTIR spectroscopy was used to maintain the identification of RME's functional chemical groups that were engaged in the reduction reaction that produced AgNPs (Fig. 4). The peaks at 1433 cm^{-1} reflect polyphenols and aromatic chemicals, whereas the peaks at 3376, 2929, and 1648 cm^{-1} represent acidic OH, C aliphatic, and C=O of phenolic acids and flavonoids, respectively. The peak at 1075 cm^{-1} validated the RME's secondary OH groups. The spectrum of RME-AgNPs showed the same peaks indicating that the compounds in the extract capped the AgNPs, but with a much lower intensity due to the involvement of the extract's functional groups in the bio-reduction process.[12]

3.2.3. XRD. The crystallinity of the synthesized silver nanoparticles using RME was examined by X-ray diffraction (XRD), herein, the biogenic RME-AgNPs exhibited peaks with 2*θ* values at 38.34°, 44.29°, and 64.65°. These values correspond to

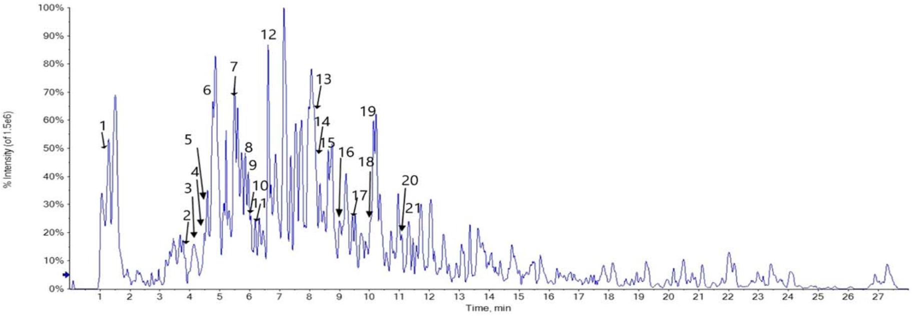

Fig. 1 LC/MS/MS chromatogram of *Retama monosperma* root extract in the negative ion mode.

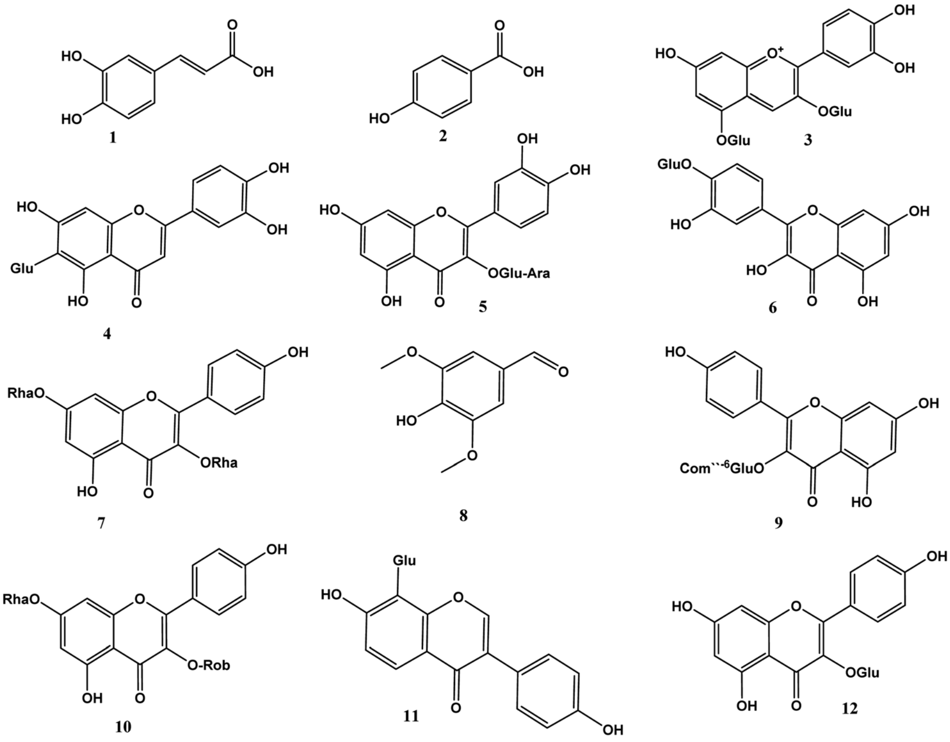

Fig. 2 Structures of some identified compounds from *Retama monosperma* extract.

Table 1 Phenolic compounds tentatively identified from the *Retama monosperma* extract in the negative ion mode

No.	Compound	RT (min)	Precursor *m*/*z*	Product ions M_s/M_s	Molecular formula	Ref.
1	Caffeic acid	1.29	179.05	153.02, 135.11	$C_9H_8O_4$	28
2	*p*-Hydroxybenzoic acid	3.98	137.02	93.04	$C_7H_6O_3$	29
3	Cyanidin-3,5-di-*O*-glucoside	4.41	609.15	447.01, 285.33	$C_{27}H_{31}O_{16}$	30
4	Luteolin-6-*C*-glucoside	4.60	447.05	285.42	$C_{21}H_{20}O_{11}$	31
5	Quercetin-3-*O*-arabinoglucoside	4.61	595.02	433.01, 301.05	$C_{26}H_{28}O_{16}$	30
6	Quercetin-4′-glucoside	4.82	463.12	301.07	$C_{21}H_{20}O_{12}$	30
7	Kaempferol-3,7-*O*-bis-alpha-L-rhamnoside	5.72	577.16	431.13, 285.06	$C_{27}H_{30}O_{14}$	30
8	Syringaldehyde	5.98	181.05	166.73	$C_9H_{10}O_4$	32
9	Kaempferol-3-*O*-(6′′′′-*p*-coumaroyl)-glucoside	6.03	593.15	477.11, 285.04	$C_{30}H_{26}O_{13}$	3
10	Kaempferol-3-*O*-robinoside-7-*O*-rhamnoside	6.15	739.21	593.02, 430.78	$C_{33}H_{40}O_{19}$	33
11	Daidzein-8-*C*-glucoside	6.43	415.10	379.14, 249.03	$C_{21}H_{20}O_9$	34
12	Kaempferol-3-*O*-glucoside	6.66	447.09	285.04	$C_{21}H_{20}O_{11}$	35
13	Myricitrin	8.34	463.15	271.13, 151.06	$C_{21}H_{20}O_{12}$	36
14	Kaempferol-7-neohesperidoside	8.45	593.05	447.0, 284.80	$C_{27}H_{30}O_{15}$	37
15	Acacetin-7-*O*-rutinoside	8.57	591.15	455.08, 249.11	$C_{28}H_{32}O_{14}$	38
16	Kaempferol-3-*O*-alpha-L-rhamnoside	9.19	431.10	285.03, 179.01	$C_{21}H_{20}O_{10}$	39
17	Quercetin	9.89	301.10	273.26, 178.95	$C_{15}H_{10}O_7$	40
18	Luteolin	9.92	285.04	151.03, 133.10	$C_{15}H_{10}O_6$	40
19	Apigenin	10.24	269.0462	254.05, 225.04	$C_{15}H_{10}O_5$	41
20	Acacetin	11.11	283.0247	273.09, 257.05	$C_{16}H_{12}O_5$	42
21	Naringenin	11.31	271.0604	185.09	$C_{15}H_{12}O_5$	43

the planes at (111), (200), and (220) for the face-centered cubic AgNPs (Fig. 5).

3.2.4. High-resolution transmission electron microscope (TEM). HR-TEM was employed to measure the particle size and shape of RME-AgNPs, the RME-AgNP colloid material was dispersed in distilled water and focused by the microscope grid, and the resulting image displayed the spherical nature of RME-AgNPs with a particle size ranging from 9.87 to 21.16 nm with an average particle size of 13.22 nm (Fig. 6A).

3.2.5. Scanning electron microscope. The surface images of a material can be examined using SEM. The particle distribution, size, and shape in the subject matter can be precisely described. It can also determine the morphological properties of the material being studied and whether it belongs to the

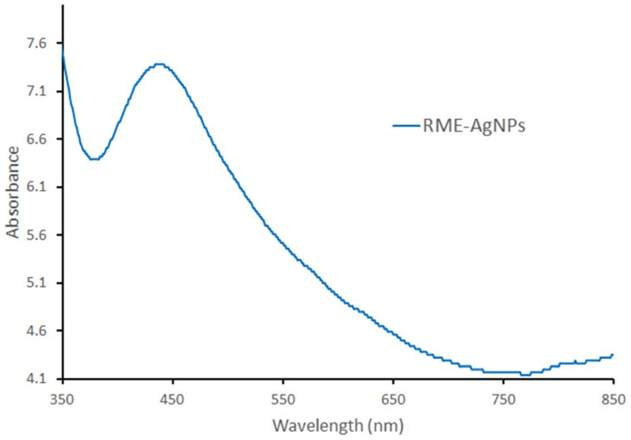

Fig. 3 UV spectra of green-synthesized AgNPs using RME (RME-AgNPs).

micro- or nanoscale. SEM analysis revealed the spherical shape and propensity to combine the green-synthesized AgNPs and prominent silver ions with a mass% of 71.14 ± 0.57 (Fig. 6B).

3.2.6. **Zeta potential.** Zeta potential is an analysis tool to detect the nanometal stability by measuring the charge of formed nanoparticles. The zeta potential of the RME-AgNPs was −15.25 mV, which reflected good nanoparticle stability (Fig. 7).

3.3. Microbiology study

3.3.1. **Antibacterial assays.** The results of the antibacterial activity of RME root extract and green-synthesized AgNPs against Gram-positive bacteria (*S. aureus*, *B. subtilis*) and Gram-negative bacteria (*E. coli*, *P. aeruginosa*) by the disc diffusion method are presented in Table 2. It was found that the RME root extract and RME-AgNPs had significant antibacterial activity against bacterial pathogens under investigation. However, AgNPs revealed a higher efficacy against Gram-positive and Gram-negative bacteria than that of the RME root extract.

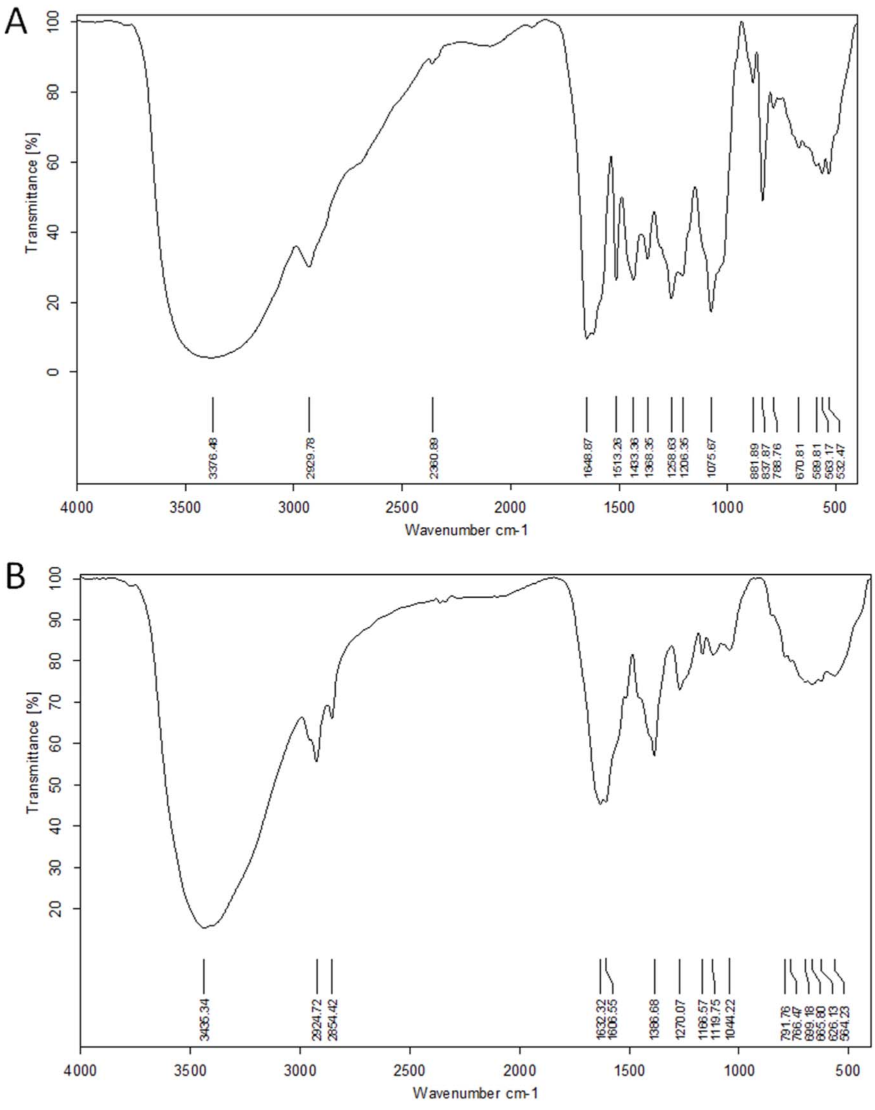

Fig. 4 FTIR spectrum of (A) RME and (B) RME-AgNPs.

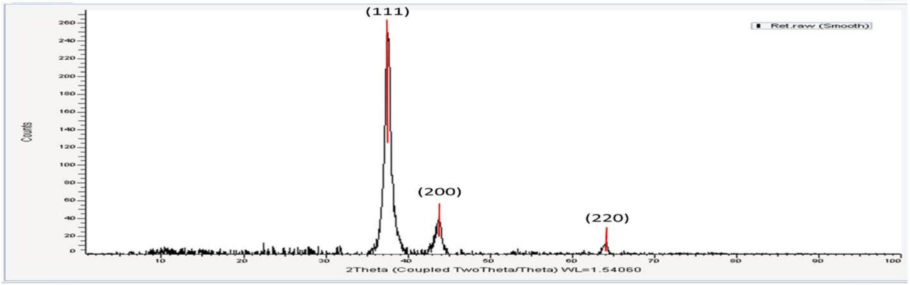

Fig. 5 XRD chromatogram of RME-AgNPs.

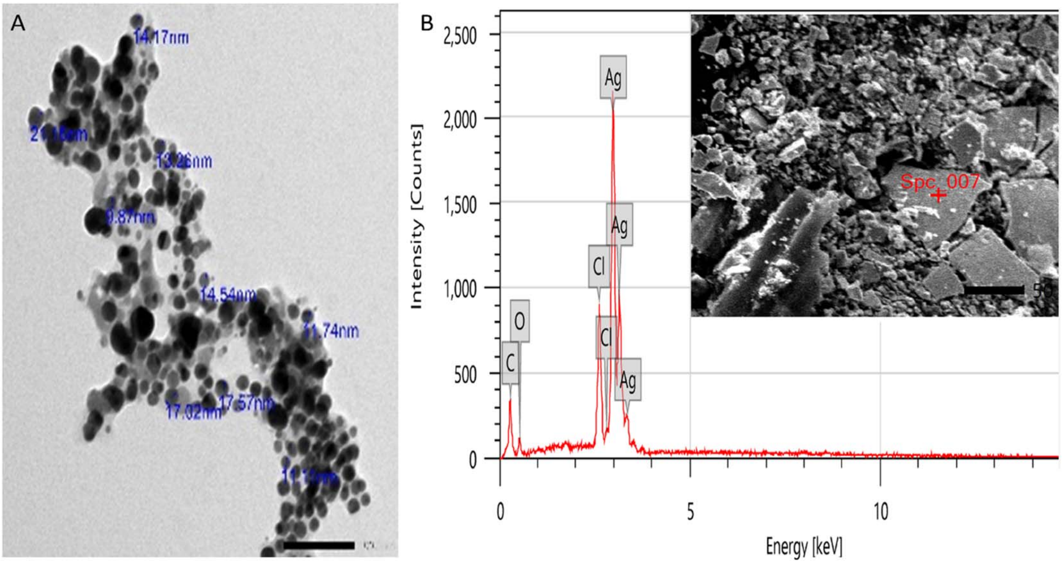

Fig. 6 Electron microscopy photos of RME-AgNPs: (A) HR-TEM and (B) SEM.

Further investigation of the antibacterial activity was performed by MIC and MBC assays. The RME-AgNPs revealed the best antibacterial properties against all bacterial strains under investigation, with the MIC and MBC values ranging from 64 to 512 μg mL^{-1}. The corresponding values for the RME range from 512 to 2048 μg mL^{-1}.

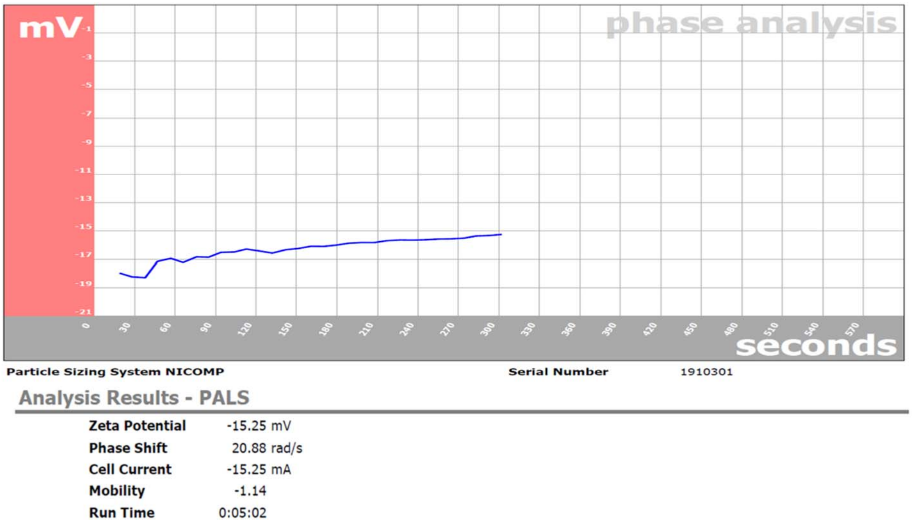

Particle Sizing System NICOMP Serial Number 1910301

Analysis Results - PALS

Zeta Potential	-15.25 mV
Phase Shift	20.88 rad/s
Cell Current	-15.25 mA
Mobility	-1.14
Run Time	0:05:02

Fig. 7 Zeta potential of RME-AgNPs.

Table 2 Disc diffusion, MIC, and MBC (μg mL^{-1}) of RME extract and RME-AgNPs against bacterial pathogens[a]

Bacterial strains	*R. monosperma* extract Diameter of inhibition zone (mm) ± SD	*R. monosperma* extract MIC (μg mL^{-1})	*R. monosperma* extract MBC (μg mL^{-1})	*R. monosperma* AgNPs Diameter of inhibition zone (mm) ± SD	*R. monosperma* AgNPs MIC (μg mL^{-1})	*R. monosperma* AgNPs MBC (μg mL^{-1})	Positive control Diameter of inhibition zone (mm) ± SD	Positive control MIC (μg mL^{-1})
Gram-positive								
Pseudomonas aeruginosa	17.0 ± 0.0	512	512	26.0 ± 0.0	64	64	24.0 ± 0.0	128
Escherichia coli	18.0 ± 0.5	512	1024	24.0 ± 0.0	128	128	28.0 ± 0.0	64
Klebsiella pneumoniae	15.0 ± 0.0	1024	1024	20.0 ± 0.0	512	512	22.0 ± 0.0	256
Serratia marcescens	15.0 ± 0.0	1024	1024	19.0 ± 0.0	512	512	22.0 ± 0.0	256
Gram-negative								
Staphylococcus aureus	12.0 ± 0.0	2048	2048	20.0 ± 0.0	512	512	22.0 ± 0.0	256
Bacillus subtilis	14.0 ± 0.0	1024	1024	22.0 ± 0.0	512	512	25.0 ± 0.0	128

[a] MIC: minimum inhibitory concentration; MBC: minimum bactericidal concentration. Ampicillin (10 mg mL^{-1}) was used as a positive control. The values represent the mean of the inhibition zone diameter (mm) ± standard deviation (SD).

3.3.2. Time-killing assay of green-synthesized AgNPs. The influences of the exposure of bacterial pathogens to RME-AgNPs were investigated by measuring the growth at different time intervals. The growth of the control strains (untreated) increased rapidly during incubation periods. The 0.5 × MIC of the AgNPs revealed a slowing down in the growth of the pathogens. A significant inhibition in the growth was observed when the pathogens were treated with 1 and 2 × MIC values (Fig. 8).

3.3.3. Scanning electron microscopy (SEM) of bacteria. SEM was performed to investigate the interaction of RME-AgNPs with bacterial cells. SEM micrographs showed the surface of untreated bacterial cells as smooth and intact. However, significant morphological changes were observed in bacterial cells treated with RME-AgNPs (Fig. 9). The bacterial cell wall of *B. subtilis* and *P. aeruginosa* revealed severe damage, irregular shapes, and deformation, resulting in cell lysis and leakage of cytoplasmic constituents. *E. coli* strain reveals big holes that resulted in lysed cells. Moreover, the *S. aureus* cell wall exhibited small pores, suggesting that this strain was more resistant to RME-AgNP treatment than other bacterial strains under investigation.

3.4. Network pharmacology studies

3.4.1. Plant-compound networks. A network connecting the *Retama monosperma* plant to 21 compounds identified tentatively from the plant is the plant-compound network.

3.4.2. Compound-target networks. The formed network connected the identified compounds to their annotated targets, consisting of 287 nodes: representing the identified compounds and the targets. There are 927 edges representing the correlation between the compounds and targets, with a characteristic path length of 2.882 and network centralization of 0.524.

3.4.3. Complete network pharmacology. The complete network pharmacology results upon merging the plant-compound network and compound-target networks. The formed network consisted of 288 nodes and 948 edges with a characteristic path length of 2.863 and network centralization of 0.525 (Fig. 10).

3.4.4. Target-bacterial infection networks. All 266 targets were entered into the DisGeNET database, and a summary of 47 328 gene-disease associations was obtained. Upon filtration of the results, to focus on bacterial infections, 41 genes were found to be associated with 14 unique bacterial infections. The formed gene-bacterial infection network comprised 55 nodes and 81 edges. The top gene in the identified gene set was TNF, with 13 associations with different bacterial infections, followed by CASP1, IL2, MPO, and F2, with 6, 5, 4, and 4 associations, respectively (Fig. 11).

3.4.5. Infection target-compound networks. A network connecting the targets of the identified gene set related to common bacterial infections and their corresponding compounds of *Retama monosperma* identified compounds. The formed network is called the infection target-compound network and 18 compounds were found to be related to 41 targets related to bacterial infection.

3.4.6. Infection–infection target-compound networks. The network consisted of 71 nodes and 246 edges with

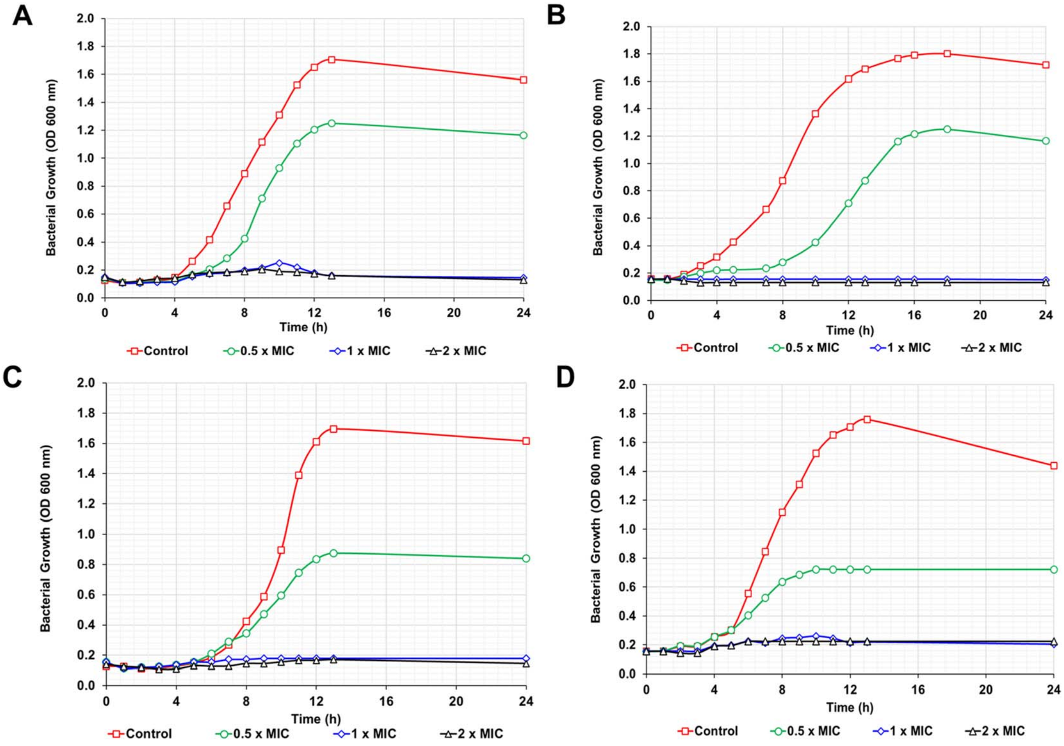

Fig. 8 Time–kill curve plots for (A) *S. aureus*, (B) *B. subtilis*, (C) *E. coli*, and (D) *P. aeruginosa* after exposure to 0.5 × MIC, 1 × MIC, and 2 × MIC values of RME-AgNPs. The growth was recorded hourly at OD_{600} for 24 h.

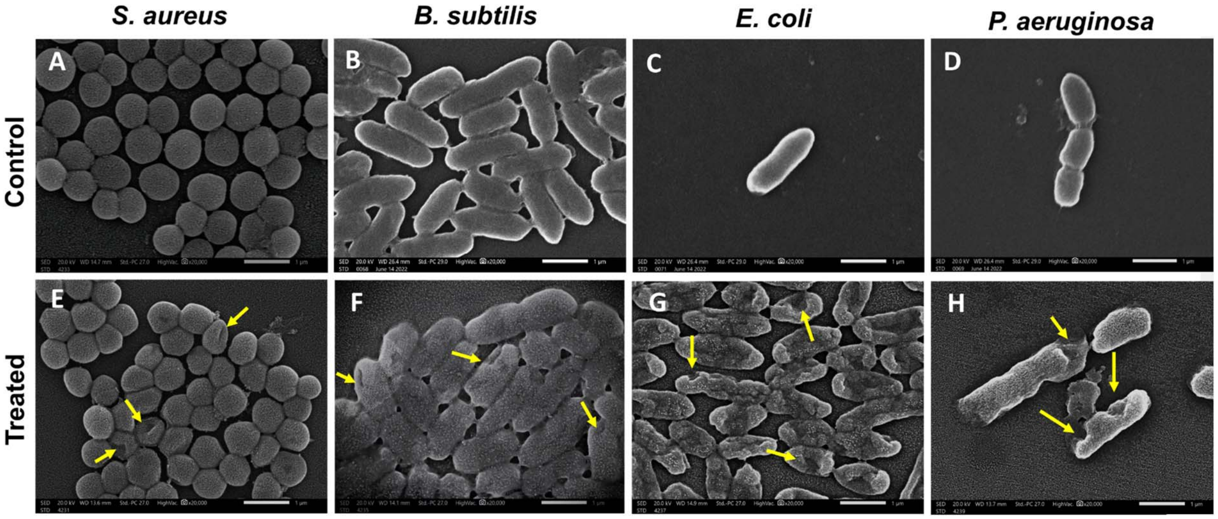

Fig. 9 Scanning electron microscopy (SEM) of control (untreated) (A–D) and treated bacteria (E–H) with RME-AgNPs after 12 h of treatment. (A & E) *S. aureus*, (B & F) *B. subtilis*, (C & G) *E. coli*, and (D & H) *P. aeruginosa*. The arrows indicate the shrinking, pore formation and deformation of bacterial cell walls. Scale bar = 1 μm and magnification power of 20 000×.

a characteristic path length of 2.538 and network centralization of 0.339. In this network, the compounds were arranged in a degree sorted layout to find out the top compounds related to infections. The top compounds were luteolin, quercetin, acacetin and apigenin with 30, 29, 24 and 22 edges, respectively (Fig. 12).

3.4.7. Target gene-pathway networks. To investigate the probable pathways of RME on bacterial infections, the pathway enrichment of 41 probable targets involved in bacterial infections were targeted by 21 identified compounds interacting with bacterial infections using the KEGG and ShinyGO databases. The pathway analysis illustrated the top 24 pathways annotated by the target genes. Upon focusing on the pathways involved in bacterial infections, three pathways were identified as the top pathways according to a number of genes: pathways in cancer,

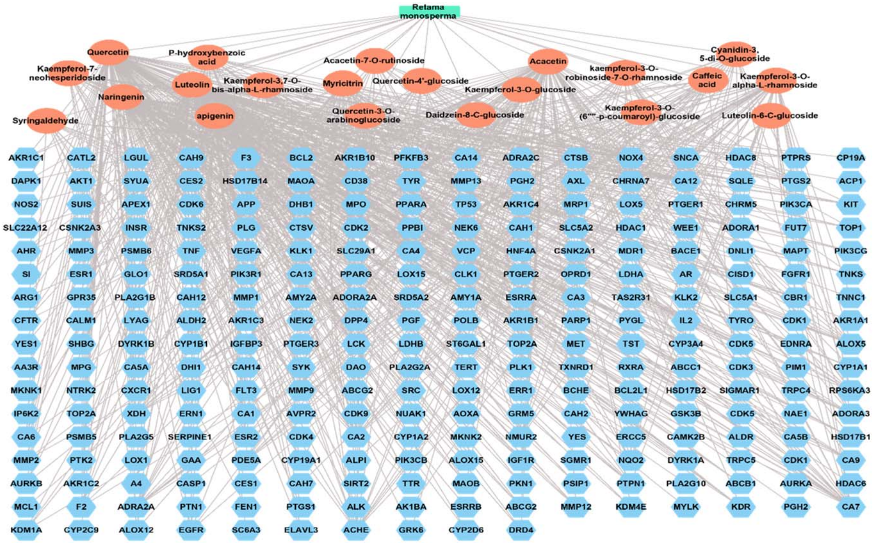

Fig. 10 Complete network pharmacology, a network that links the plant *Retama monosperma* with the identified compounds and annotated targets. Green rectangle is the plant name, orange oval shapes represent the identified compounds, and blue heptagonal shapes represent the targets.

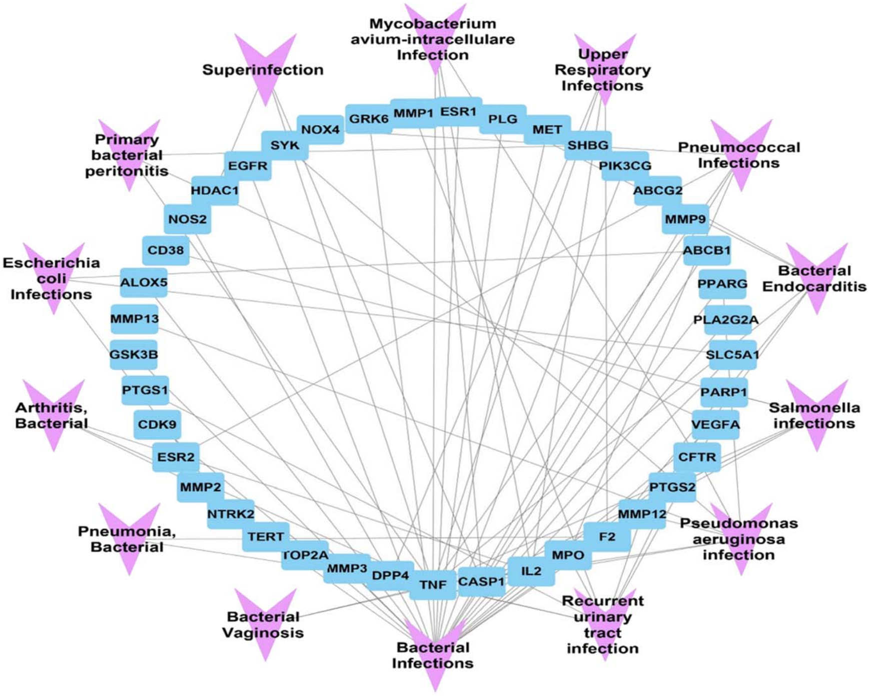

Fig. 11 Target-bacterial infection network; a network that links the targets to bacterial infections. Blue rectangles represent targets related to bacterial infections; pink arrowheads represent types of bacterial infections.

PI3K-Akt signaling pathway, and Relaxin signaling pathway. Top 20 pathways are illustrated in the plot diagram (Fig. 13), and diagrams of the top two KEGG pathways are illustrated in Fig. 14.

3.4.8. GO enrichment analysis.

The gene ontology of the RME targets related to microbial infections is described in terms of biological processes, cellular components, and molecular function. The major identified biological processes according to fold enrichment are cellular response to UV-A, response to UV-A and cyclooxygenase pathway. Under the same arrangement order, the top cellular components are the apical plasma membrane, apical part of cells, and extracellular matrix. The top molecular functions are transcription coactivator binding, ABC-type xenobiotic transporter activity, and efflux transmembrane transporter activity (Fig. 15).

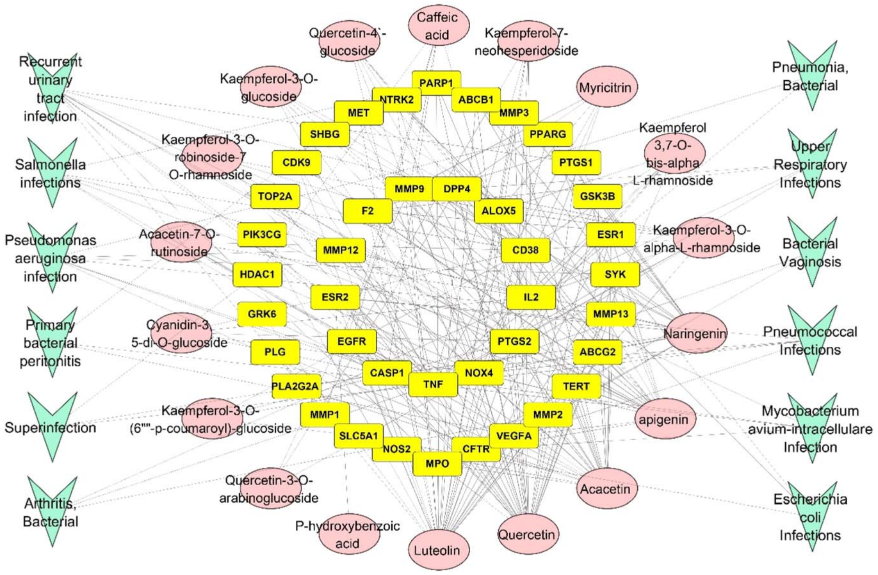

Fig. 12 Infection–infection target-compound network: a network connecting different types of bacterial infections with infection targets and with the identified compounds, green arrowheads represent types of bacterial infections, yellow rectangles represent targets related to infections, and pink oval shapes represent the identified compounds from RME.

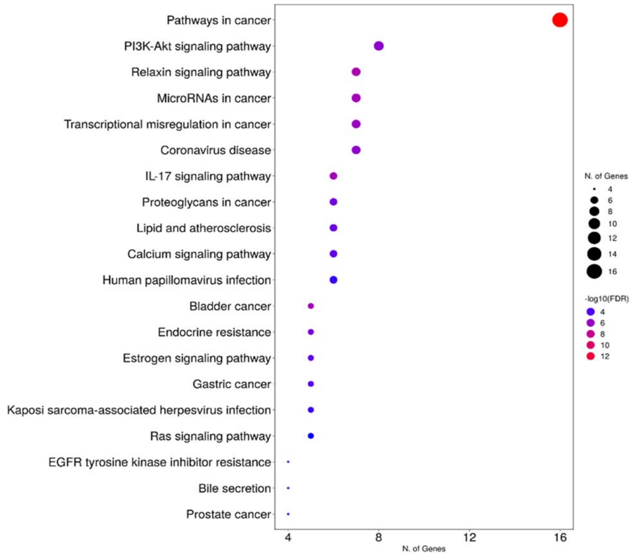

Fig. 13 Top KEGG pathways related to identified targets of RME related to bacterial infections.

3.5. Molecular docking of co-crystallized ligands and *Retama monosperma* extract 21 compounds

To validate the docking protocol, self-docking of the co-crystallized ligand (TNF-α small-molecule inhibitor co-crystallized with PDB ID: 2AZ5) was performed. As shown in Table 3, self-docking of the co-crystallized ligand scores ΔG of -6.7248 kcal mol^{-1} shows similar interactions to the reported ones where four H-bonds are formed with 3 amino acids: Gln61, Tyr119, and Gly121 in addition to a pi-cation and pi–pi interactions with Tyr119 (Table 4).

Molecular docking of the 21 compounds in the test set showed good binding affinities against TNF-α receptors ($-3.7009 < \Delta G < -6.8084$ kcal mol^{-1}) (Table 3).

Table 4 displays the 2D structure and 2D interaction of the best six scoring compounds: kaempferol-3-*O*-robinoside-7-*O*-rhamnoside, quercetin-3-*O*-arabinoglucoside, acacetin-7-*O*-rutinoside, kaempferol-7-neohesperidoside, cyanidin-3,5-di-*O*-glucoside and kaempferol-3,7-*O*-bis-alpha-L-rhamnoside with binding free energies of -6.8084, -6.5907, -6.2491, -6.0532, -6.0489 and -6.0369 kcal mol^{-1}, respectively. All ligands showed at least one pi–pi interaction with the pocket's binding site, mainly with Tyr59 or Tyr119 or with both of them. Quercetin-3-*O*-arabinoglucoside was able to form a third pi–pi interaction with His15. This main type of interaction is suggested to be responsible for the antimicrobial activity, as it is also reported in the inhibitor co-crystallized with TNF-α. Another suggested important interaction is maintaining at least one H-bond with any of the pocket's sidechains.

Although kaempferol-3-*O*-robinoside-7-*O*-rhamnoside showed the highest binding affinity towards TNF-α, we cannot consider it the main component responsible for the extract antimicrobial activity as it shows non-favorable interactions; only 2 H-bonds with no pi–pi interactions. However, although kaempferol-3,7-*O*-bis-alpha-L-rhamnoside is the least scored hit compared to the other 5 highest scored ones, it possesses the best interactions showing 2H-bonds with Leu120 and Tyr151 and a pi–pi interaction with Tyr59. Similarly, cyanidin-3,5-di-*O*-glucoside was able to maintain 2H-bonds with Leu120 and Gln149 in addition to pi–pi and pi-cation interactions with Tyr119. Another hit that shows very good interaction with a high binding score is Quercetin-3-*O*-arabinoglucoside, which interacts with the receptor *via* an H-bond with Tyr151, 3 pi–pi

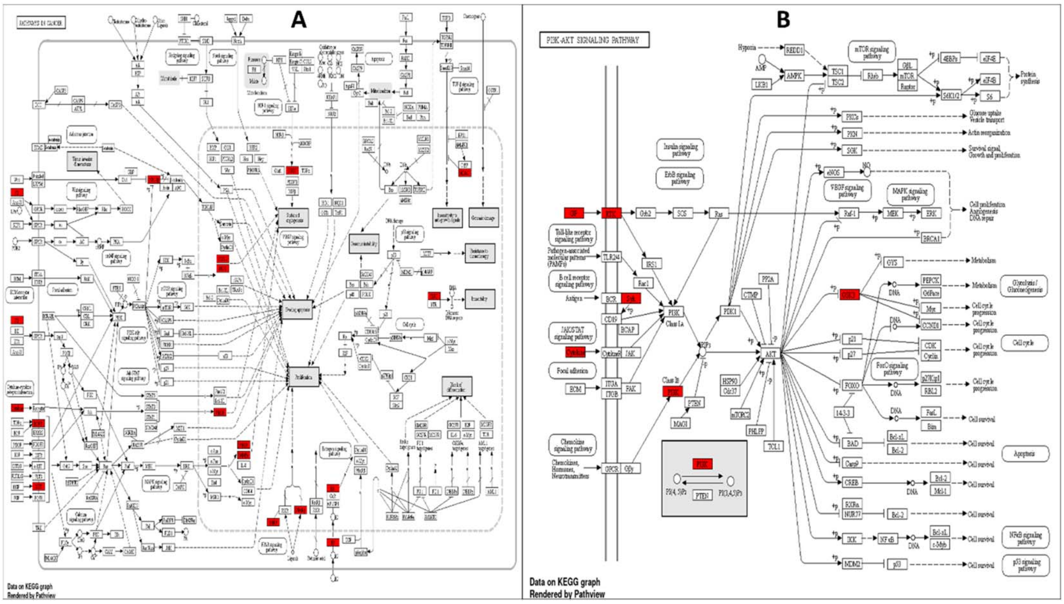

Fig. 14 KEGG diagrams of top two biological pathways; red rectangles are the target genes in each pathway: (A) pathways in cancer and (B) PI3K-Akt signaling pathway.

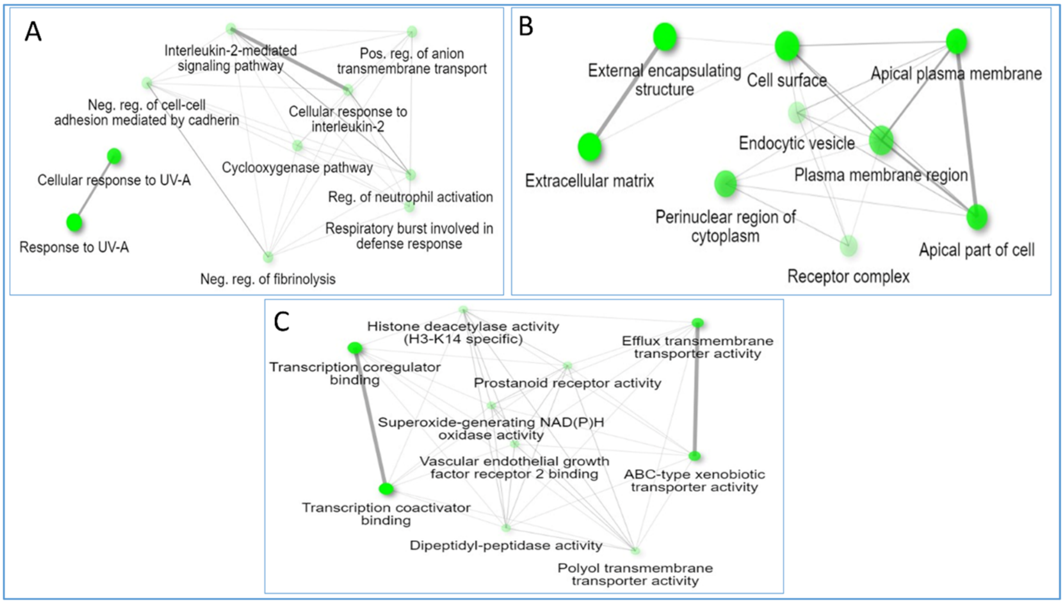

Fig. 15 Gene ontology analysis of RME targets related to infections in terms of (A) biological process, (B) cellular component, and (C) molecular functions.

interactions with His15 and Tyr59 and a pi–sigma interaction with Tyr119.

4. Discussion

Due to the need for eco-friendly antimicrobial agents, green-synthesized silver nanoparticles are considered advantageous over the other methods. AgNPs are characterized with their large surface area, which is significant in therapeutic applications.[44]

A green synthesis route of nanosilver metal formation through RME led to the formation of eco-friendly, clean, safe silver nanoparticles with no application of hazardous chemical agents. The formed RME-AgNPs, upon characterization, were revealed to have a uniform spherical shape with a particle size ranging from 9.87 to 21.16 nm and the average particle size of 13.22 nm in crystalline form, as evidenced by XRD analysis. The stability of the formed RME-AgNPs was evidenced by a negative charge measured zeta potential of −15.25 mV.

Table 3 Docking Δ*G* scores of 21 compounds of *Retama monosperma* extract on a TNF-α active pocket

Compound	Δ*G* (kcal mol^{-1})
Native	−6.7248
CAFFEIC ACID	−4.0349
p-Hydroxybenzoic acid	−3.7009
Cyanidin-3,5-di-*O*-glucoside	−6.0489
Luteolin-6-*C*-glucoside	−5.3844
Quercetin-3-*O*-arabinoglucoside	−6.5907
Quercetin-4′-glucoside	−5.2593
Kaempferol-3,7-*O*-bis-alpha-L-rhamnoside	−6.0369
Syringaldehyde	−4.3179
Kaempferol-3-*O*-(6′′′′-*p*-coumaroyl)-glucoside	−5.8349
Kaempferol-3-*O*-robinoside-7-*O*-rhamnoside	−6.8084
Daidzein-8-*C*-glucoside	−5.1642
Kaempferol-3-*O*-glucoside	−5.2014
Myricitrin	−5.3469
Kaempferol-7-neohesperidoside	−6.0532
Acacetin-7-*O*-rutinoside	−6.2491
Kaempferol-3-*O*-alpha-L-rhamnoside	−5.1377
Quercetin	−4.7668
Luteolin	−4.5788
Apigenin	−4.7450
Acacetin	−4.6155
Naringenin	−4.4981

The current study assessed novel green-synthesized AgNPs and RME root extract regarding their antibacterial activity. The results revealed that green-synthesized AgNPs had a higher antibacterial activity than that of the RME root extract. This is because AgNPs possess a positive charge that could attach better and penetrate through the cell wall membrane.[45] Furthermore, the binding of AgNPs to the bacterial cell wall proteins causes a reduction in the membrane's permeability and leakage of intracellular components, which finally leads to bacterial death.[46] In addition to the cell membrane damage, nanoparticles alter the cell function by interacting with amino acids and enzymes, causing the generation of reactive oxygen species (ROS) and misfolding of bacterial DNA.[47,48]

Disc diffusion assay revealed that Gram-positive bacteria were more resistant to AgNPs than Gram-negative bacteria. Previous research has reported this due to the different cell wall structures.[49,50] In Gram-negative bacteria, a 1–3 μm-thick layer of lipopolysaccharides and a 8 nm-thick layer of peptidoglycan cover the cells, facilitating the diffusion of AgNP ions into the cells. However, Gram-positive bacteria have a thicker protective peptidoglycan layer that stretches over 80 nm. Thus, the damage in Gram-negative bacteria upon the interaction of AgNPs with cell walls becomes more harmful than Gram-positive strains due to the absence of the thick protective layer of peptidoglycan.[7]

SEM investigated the bactericidal mechanism of RME-AgNPs. The visualization of bacterial cell walls of *B. subtilis*, *E. coli*, and *P. aeruginosa* revealed severe damage and deformation. Moreover, the *S. aureus* cell wall exhibited small pores. The SEM micrographs confirmed that green-synthesized AgNPs penetrate the bacterial cells, resulting in membrane disruption, which may shrink the cell and result in cell lysis.[51]

Table 4 Ligands' name, chemical structure and 2D interactions with their receptors

Ligand name and chemical structure	Ligand interactions with the enzyme active site
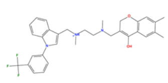 Co-crystallized inhibitor	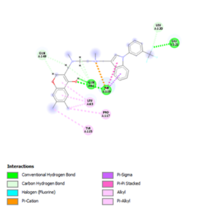
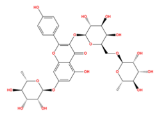 kaempferol-3-O-robinoside-7-O-rhamnoside	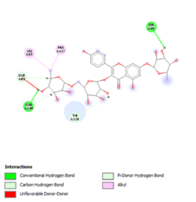
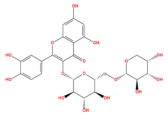 Quercetin-3-O-arabinoglucoside	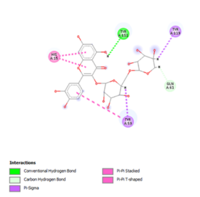
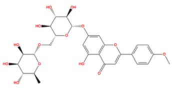 Acacetin-7-O-rutinoside	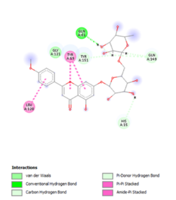
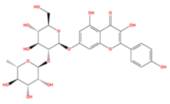 Kaempferol-7-neohesperidoside	
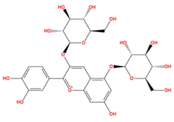 Cyanidin-3, 5-di-O-glucoside	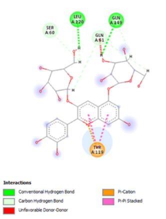
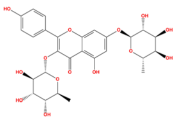 Kaempferol-3,7-O-bis-alpha-L-rhamnoside	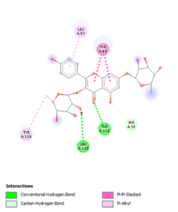

The natural green source used for synthesizing metal nanoparticles contributes to controlling the formed nanometal physicochemical characteristics and their medical applications.[14] Thus, the bioinformatic study was employed to find out the top genes of the whole gene set, which is responsible for the antimicrobial activities and the top genes were determined as TNF genes. For explanation of the exact compounds among all the 21 identified compounds from RME responsible for antimicrobial potential, a network pharmacology design was constructed in a backward way, and the top compounds contributing to antimicrobial infections were defined as luteolin, quercetin, acacetin, and apigenin with 30, 29, 24 and 22 edges, respectively.

Molecular docking study identified 6 out of 21 compounds of *Retama monosperma* extract that scored the highest binding affinities with similar ΔG scores to those of co-crystallized inhibitors. Such compounds were kaempferol-3-*O*-robinoside-7-*O*-rhamnoside, quercetin-3-*O*-arabinoglucoside, acacetin-7-*O*-rutinoside, kaempferol-7-neohesperidoside, cyanidin-3,5-di-*O*-glucoside and kaempferol-3,7-*O*-bis-alpha-L-rhamnoside, and they were so much likely to be responsible for the biological activity (antimicrobial activity) of *Retama monosperma* extract.

5. Conclusion

Retama monosperma roots are natural excellent bio-reductants and capping agents for the green synthesis of silver nanoparticles with outstanding physicochemical features. The formed AgNPs exhibited a remarkably high antibacterial activity towards Gram-positive and Gram-negative bacteria and could be introduced as promising bactericidal agents in topical antimicrobial pharmaceutical preparations.

Conflicts of interest

There are no conflicts to declare.

Acknowledgements

The authors are thankful to the Deanship of Scientific Research at Najran University for funding this work, under the General Research Funding program grant code (NU/DRP/MRC/12/40).

References

1 D. Byarugaba, Antimicrobial resistance in developing countries and responsible risk factors, *Int. J. Antimicrob. Agents*, 2004, **24**(2), 105–110.

2 M. A. Cooper and D. Shlaes, Fix the antibiotics pipeline, *Nature*, 2011, **472**(7341), 32.

3 B. Alotaibi, *et al.*, Antimicrobial activity of Brassica rapa L. flowers extract on gastrointestinal tract infections and antiulcer potential against indomethacin-induced gastric ulcer in rats supported by metabolomics profiling, *J. Inflammation Res.*, 2021, **14**, 7411.

4 H. M. E.-S. Azzazy, A. M. Sawy, A. Abdelnaser, M. R. Meselhy, T. Shoeib and S. A. Fahmy, *Peganum harmala* Alkaloids and Tannic Acid Encapsulated in PAMAM Dendrimers: Improved Anticancer Activities as Compared to Doxorubicin, *ACS Appl. Polym. Mater.*, 2022, **4**, 7228–7239.

5 N. K. Sedky, N. M. Abdel-Kader, M. Y. Issa, M. M. M. Abdelhady, S. N. Shamma, U. Bakowsky and S. A. Fahmy, Co-Delivery of Ylang Ylang Oil of *Cananga odorata* and Oxaliplatin Using Intelligent pH-Sensitive Lipid-Based Nanovesicles for the Effective Treatment of Triple-Negative Breast Cancer, *Int. J. Mol. Sci.*, 2023, **24**, 8392, DOI: **10.3390/ijms24098392**.

6 S. A. Fahmy, K. A. Nematallah, N. K. Mahdy, H. I. El-Askary, M. R. Meselhy and H. M. El-Said Azzazy, Enhanced antioxidant, antiviral, and anticancer activities of the extract of fermented Egyptian rice bran complexed with hydroxypropyl-β-cyclodextrin, *ACS Omega*, 2022, **7**, 19545–19554.

7 O. T. Fanoro and O. S. Oluwafemi, Bactericidal antibacterial mechanism of plant synthesized silver, gold and bimetallic nanoparticles, *Pharmaceutics*, 2020, **12**(11), 1044.

8 L. Boulos, *Flora of Egypt*, Al Hadara Publishing, Cairo, 1999, pp. 1–419.

9 R. B. Garden and P. Kew, *Plants of the world online*, Obtenido de Royal Botanic Garden, 2022, **https://www.plantsoftheworldonline.org/taxon/urn:lsid:ipni**.

10 A. León-González, *et al.*, Genus Retama: A review on traditional uses, phytochemistry, and pharmacological activities, *Phytochem. Rev.*, 2018, **17**, 701–731.

11 F. Z. Benkhouili, *et al.*, *Retama monosperma (L.) Boiss: A review of its uses in traditional medicine, chemical constituents, and pharmacologic activities.* Phytomedicine Plus, 2022, p. 100349.

12 S. A. Fahmy, I. M. Fawzy, B. M. Saleh, M. Y. Issa, U. Bakowsky and H. M. E.-S. Azzazy, Green Synthesis of Platinum and Palladium Nanoparticles Using *Peganum harmala* L. Seed Alkaloids: Biological and Computational Studies, *Nanomaterials*, 2021, **11**, 965, DOI: **10.3390/nano1104096513**.

13 B. Alotaibi, *et al.*, Antibacterial activity of nano zinc oxide green-synthesised from Gardenia thailandica triveng. Leaves against Pseudomonas aeruginosa clinical isolates: In vitro and in vivo study, *Artif. Cells, Nanomed., Biotechnol.*, 2022, **50**(1), 96–106.

14 F. A. Mokhtar, *et al.*, Green Biosynthesis of Silver Nanoparticles Using Annona glabra and Annona squamosa Extracts with Antimicrobial, Anticancer, Apoptosis Potentials, Assisted by In Silico Modeling, and Metabolic Profiling, *Pharmaceuticals*, 2022, **15**(11), 1354.

15 S. A. Fahmy, A. Ramzy, A. A. Mandour, S. Nasr, A. Abdelnaser, U. Bakowsky and H. M. E.-S. Azzazy, PEGylated Chitosan Nanoparticles Encapsulating Ascorbic Acid and Oxaliplatin Exhibit Dramatic Apoptotic Effects against Breast Cancer Cells, *Pharmaceutics*, 2022, **14**, 407, DOI: **10.3390/pharmaceutics14020407**.

16 S. A. Fahmy, N. K. Mahdy, H. Al Mulla, A. N. ElMeshad, M. Y. Issa and H. M. E.-S. Azzazy, PLGA/PEG Nanoparticles Loaded with Cyclodextrin-*Peganum harmala* Alkaloid Complex and Ascorbic Acid with Promising Antimicrobial Activities, *Pharmaceutics*, 2022, **14**, 142, DOI: **10.3390/pharmaceutics14010142**.

17 A. Bauer, M. Turck, *et al.*, Antibiotic susceptibility testing by a standardized single disk method, *Am. J. Clin. Pathol.*, 1966, **45**(4), 493.

18 CLSI, *Performance Standards for Antimicrobial Susceptibility Testing, CLSI supplement M100*, Clinical and Laboratory Standards Institute, Wayne, PA, 28th edn, vol. 38, 2018.

19 S. Kim, *et al.*, PubChem substance and compound databases, *Nucleic Acids Res.*, 2016, **44**(D1), D1202–D1213.

20 U. Consortium, UniProt: a hub for protein information, *Nucleic Acids Res.*, 2015, **43**(D1), D204–D212.

21 D. Gfeller, *et al.*, SwissTargetPrediction: a web server for target prediction of bioactive small molecules, *Nucleic Acids Res.*, 2014, **42**(W1), W32–W38.

22 J. Piñero, *et al.*, The DisGeNET knowledge platform for disease genomics: 2019 update, *Nucleic Acids Res.*, 2020, **48**(D1), D845–D855.

23 S. X. Ge, D. Jung and R. Yao, ShinyGO: a graphical gene-set enrichment tool for animals and plants, *Bioinformatics*, 2020, **36**(8), 2628–2629.

24 N. M. O'Boyle, *et al.*, Open Babel: An open chemical toolbox, *J. Cheminf.*, 2011, **3**(1), 1–14.

25 R. Huey and G. M. Morris, *Using AutoDock 4 with AutoDocktools: a tutorial*, The Scripps Research Institute, USA, 2008, vol. 54, p. 56.

26 I. Kufareva and R. Abagyan, Methods of protein structure comparison. *Homology Modeling: Methods and Protocols*, 2012, pp. 231–257.

27 J. Fuhrmann, *et al.*, A new Lamarckian genetic algorithm for flexible ligand-receptor docking, *J. Comput. Chem.*, 2010, **31**(9), 1911–1918.

28 X. Wang, *et al.*, Simultaneous determination of caffeic acid and its major pharmacologically active metabolites in rat plasma by LC-MS/MS and its application in pharmacokinetic study, *Biomed. Chromatogr.*, 2015, **29**(4), 552–559.

29 S. Tsuruda, T. Sakamoto and K. Akaki, Simultaneous determination of twelve sweeteners and nine preservatives in foods by solid-phase extraction and LC-MS/MS, *Shokuhin Eiseigaku Zasshi*, 2013, **54**(3), 204–212.

30 E. E. Eltamany, *et al.*, Chemical profiling, antioxidant, cytotoxic activities and molecular docking simulation of Carrichtera annua DC.(Cruciferae), *Antioxidants*, 2020, **9**(12), 1286.

31 P. Geng, *et al.*, Comprehensive characterization of C-glycosyl flavones in wheat (Triticum aestivum L.) germ using UPLC-PDA-ESI/HRMSn and mass defect filtering, *J. Mass Spectrom.*, 2016, **51**(10), 914–930.

32 J. Prothmann, *et al.*, Ultra-high-performance supercritical fluid chromatography with quadrupole-time-of-flight mass spectrometry (UHPSFC/QTOF-MS) for analysis of lignin-derived monomeric compounds in processed lignin samples, *Anal. Bioanal. Chem.*, 2017, **409**, 7049–7061.

33 R. E. March, X. S. Miao and C. D. Metcalfe, A fragmentation study of a flavone triglycoside, kaempferol-3-O-robinoside-7-O-rhamnoside, *Rapid Commun. Mass Spectrom.*, 2004, **18**(9), 931–934.

34 A. A. Carvalho, *et al.*, First report of flavonoids from leaves of Machaerium acutifolium by DI-ESI-MS/MS, *Arabian J. Chem.*, 2022, **15**(5), 103765.

35 S. S. El-Hawary, *et al.*, Jasminum azoricum L. leaves: HPLC-PDA/MS/MS profiling and in-vitro cytotoxicity supported by molecular docking, *Nat. Prod. Res.*, 2021, **35**(23), 5518–5520.

36 N. A. Latiff, *et al.*, Liquid chromatography tandem mass spectrometry for the detection and validation of quercetin-3-O-rutinoside and myricetin from fractionated Labisia pumila var. Alata, *Malaysian J. Anal. Sci.*, 2018, **22**(5), 817–827.

37 Y. Chen, *et al.*, Characterization and quantification by LC-MS/MS of the chemical components of the heating products of the flavonoids extract in pollen typhae for transformation rule exploration, *Molecules*, 2015, **20**(10), 18352–18366.

38 F. S. M. Mahrous, H. Mohammed and R. Sabour, LC-ESI-QTOF-MS/MS of Holoptelea integrifolia (Roxb.) Planch. leaves and In silico study of phenolic compounds' antiviral activity against the HSV1 virus, *Azhar International Journal of Pharmaceutical and Medical Sciences*, 2021, **1**(3), 91–101.

39 L. F. Ibrahim, *et al.*, Flavonoid investigation, LC–ESIMS profile and cytotoxic activity of Raphanus raphanistrum L.(Brassicaceae), *J. Chem. Pharm. Res.*, 2016, **8**(7), 786–793.

40 A. A. Chernonosov, E. A. Karpova and E. M. Lyakh, Identification of phenolic compounds in Myricaria bracteata leaves by high-performance liquid chromatography with a diode array detector and liquid chromatography with tandem mass spectrometry, *Rev. Bras. Farmacogn.*, 2017, **27**, 576–579.

41 N. G. Attallah, *et al.*, Mechanistic insights on the in vitro antibacterial activity and in vivo hepatoprotective effects of salvinia auriculata aubl against methotrexate-induced liver injury, *Pharmaceuticals*, 2022, **15**(5), 549.

42 C. Cortés, *et al.*, Phenolic profile, antioxidant and enzyme inhibition properties of the chilean endemic plant Ovidia pillopillo (Gay) meissner (Thymelaeaceae), *Metabolites*, 2022, **12**(2), 90.

43 X. Xiong, *et al.*, Development and Validation of a Sensitive Liquid Chromatography–Tandem Mass Spectrometry Method for the Determination of Naringin and Its Metabolite, Naringenin, in Human Plasma, *J. Chromatogr. Sci.*, 2014, **52**(7), 654–660.

44 M. Ovais, *et al.*, Wound healing applications of biogenic colloidal silver and gold nanoparticles: recent trends and future prospects, *Appl. Microbiol. Biotechnol.*, 2018, **102**, 4305–4318.

45 F. Monedeiro, *et al.*, Monitoring of bactericidal effects of silver nanoparticles based on protein signatures and VOC emissions from Escherichia coli and selected salivary bacteria, *J. Clin. Med.*, 2019, **8**(11), 2024.

46 M. Seong and D. G. Lee, Silver nanoparticles against Salmonella enterica serotype typhimurium: role of inner membrane dysfunction, *Curr. Microbiol.*, 2017, **74**, 661–670.

47 C. Liao, Y. Li and S. C. Tjong, Bactericidal and cytotoxic properties of silver nanoparticles, *Int. J. Mol. Sci.*, 2019, **20**(2), 449.

48 A. Rónavári, *et al.*, Biological activity of green-synthesized silver nanoparticles depends on the applied natural extracts: a comprehensive study, *Int. J. Nanomed.*, 2017, **12**, 871.

49 Q. L. Feng, *et al.*, A mechanistic study of the antibacterial effect of silver ions on Escherichia coli and Staphylococcus aureus, *J. Biomed. Mater. Res.*, 2000, **52**(4), 662–668.

50 E. D. Cavassin, *et al.*, Comparison of methods to detect the in vitro activity of silver nanoparticles (AgNP) against multidrug resistant bacteria, *J. Nanobiotechnol.*, 2015, **13**(1), 1–16.

51 M. Yasir, D. Dutta and M. D. Willcox, Mode of action of the antimicrobial peptide Mel4 is independent of Staphylococcus aureus cell membrane permeability, *PLoS One*, 2019, **14**(7), e0215703.